Lawrence Berkeley National Laboratory

Title

A Nanoscale Ternary Amide-rGO Composite with Boosted Kinetics for Reversible H2 Storage

Permalink

https://escholarship.org/uc/item/5hk8f13p

Journal

Advanced Materials Interfaces, 10(27)

ISSN

2196-7350

Authors

Dun, Chaochao

Li, Sichi

Chen, Linfeng

et al.

Publication Date

2023-09-01

DOI

10.1002/admi.202300310

Peer reviewed

A Nanoscale Ternary Amide-rGO Composite with Boosted Kinetics for Reversible H$_2$ Storage

Chaochao Dun, Sichi Li, Linfeng Chen, Robert D. Horton, Mark D. Allendorf,
Brandon C. Wood, Vitalie Stavila,* and Jeffrey J. Urban*

Metal amides are attractive candidates for hydrogen storage due to their high volumetric and gravimetric hydrogen densities. However, the sluggish kinetics and competing side reactions during hydrogen uptake and release limit their practical use. Here, a novel nanoconfined Li$_2$Mg(NH)$_2$@reduced graphene oxide (rGO) composite is presented, which is fabricated using a melt-infiltration method with a minimum weight penalty of only 2 wt.%. The presence of rGO ensures close contact between the active phases, effectively preventing aggregation during cycling process. As a result, the reversible capacity of Li$_2$Mg(NH)$_2$@rGO reaches 4.42 wt.%, with no capacity degradation observed after multiple cycling. Theoretical calculations show that rGO catalyzes the hydrogen bond cleavage at the Mg-amide/Li hydride interface, leading to local dehydrogenation hotspots and significantly improves kinetics of dehydrogenation compared to the bulk counterpart. This study provides a promising strategy for designing metal imide-based composites to overcome the kinetic limitations and improve their reversible hydrogen storage performance.

1. Introduction

Hydrogen possesses the highest gravimetric energy density (120 MJ kg^{-1}) of any chemical fuel, and can be sustainably produced from a variety of renewable sources.[1–3] However, storage and transportation of hydrogen is challenging,[4] especially when associated with liquefaction (20–70 K) and/or compression (350–700 bar). In light of these challenges, solid-state hydrogen storage is an attractive alternative, as hydrogen-rich materials offer higher volumetric and gravimetric densities, making them well-suited to meet the evolving needs of renewable energy technologies.[5–9] Magnesium hydride (MgH$_2$) is particularly attractive for hydrogen storage systems, with high volumetric and gravimetric hydrogen densities of 110 kg H m^{-3} and 7.6 wt.%, respectively.[10,11] Unfortunately, the high desorption enthalpy (MgH$_2$⇔Mg+H$_2$) and sluggish kinetics result in a high operating temperature, which have precluded MgH$_2$ for use in certain cases, in particular for vehicular applications.[12,13] For example, the measured changes of enthalpy (ΔH) and entropy (ΔS) of nanoscale MgH$_2$ are 71.2 ± 0.5 kJ mol^{-1} H$_2$ and 129.6 ± 0.8 J K^{-1} mol^{-1} H$_2$, producing an equilibrium pressure of 1 bar at 276 °C.[14] Li—N—H system could also be used as a reversible hydrogen storage medium with a theoretical capacity up to 10.4 wt.%,[15,16] however similarly problematic thermodynamics/kinetics greatly hinder its practical applications. Irreversible generation of ammonia (NH$_3$) during decomposition, which is a poison for fuel cells, is an additional drawback of the Li—N—H system as it leads to loss of hydrogen capacity.[17] However, when amides of alkali metals and metal hydride are mixed, a synergistic destabilization of the complex hydride occurs.[18] Theoretical calculations show that substituting Mg onto the Li sites increases the electron density around the Li and H atoms, weakening the bonds between Li—N and N—H.[19] Thus, a Li—Mg amide composite could serve as a versatile H$_2$ storage material for high energy-density applications, if the problems with sluggish kinetics could be solved. Tremendous efforts have been devoted to improving the hydrogen storage properties of Li—Mg—N—H systems by adjusting compositions[20] and adding dopants, catalysts, etc.[21–23] In the Mg(NH$_2$)$_2$−2LiH composite, the absorption of hydrogen occurs as described in Reaction (1).[24] The desorption of hydrogen occurs via a two-step mechanism encompassing Reactions (2) and (3), leading to the formation of an intermediate Li$_2$Mg$_2$(NH)$_3$ phase. The overall dehydrogenation process culminates

C. Dun, L. Chen, J. J. Urban
The Molecular Foundry
Lawrence Berkeley National Laboratory
Berkeley, CA 94720, USA
E-mail: jjurban@lbl.gov
S. Li, B. C. Wood
Lawrence Livermore National Laboratory
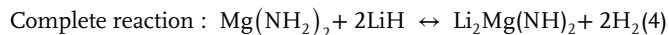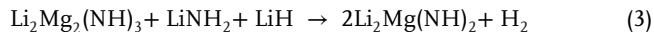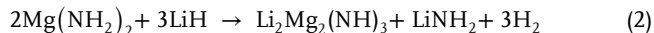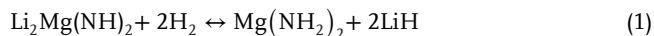7000 East Avenue, Livermore, CA 94550, USA
R. D. Horton, M. D. Allendorf, V. Stavila
Sandia National Laboratories
Livermore, CA 94550, USA
E-mail: vnstavi@sandia.gov

ADVANCED
SCIENCE NEWS

www.advancedsciencenews.com

ADVANCED
MATERIALS
INTERFACES
Open Access

www.advmatinterfaces.de

in the formation of the $Li_2Mg(NH)_2$ phase, as evidenced by Reaction (4).[25]

$$Li_2Mg(NH)_2 + 2H_2 \leftrightarrow Mg(NH_2)_2 + 2LiH \tag{1}$$

$$2Mg(NH_2)_2 + 3LiH \rightarrow Li_2Mg_2(NH)_3 + LiNH_2 + 3H_2 \tag{2}$$

$$Li_2Mg_2(NH)_3 + LiNH_2 + LiH \rightarrow 2Li_2Mg(NH)_2 + H_2 \tag{3}$$

$$\text{Complete reaction}: Mg(NH_2)_2 + 2LiH \leftrightarrow Li_2Mg(NH)_2 + 2H_2 \tag{4}$$

Nanostructing is known to alter reactive nanointerfaces,[26–28] enable reversibility,[29,30] enhance the kinetics of hydrogen storage reactions,[31–33] and decrease the required path length of the hydrogen-permeable hydride/amide layer that forms during ab/desorption.[34] Recent studies have demonstrated that the hydrogenation/dehydrogenation kinetics of $Mg(NH_2)_2$ can be greatly improved by reducing the particle size of the reactants through the use of nanostructured $Mg(NH_2)_2$ prepared via the ball-milling method.[24,35–37] In terms of controlling the nanostructure and enhancing the efficient contact between the liquid infiltrate and the template material, melt infiltration provides an alternative to classical ball-milling preparation methods, facilitating control over the nanostructure and improving the efficient contact between the liquid infiltrate and the template.[38,39] For example, Pinkerton et al. melt-infiltrated $NaAlH_4$ into 13-nm carbon aerogels and observed enhanced H_2 release kinetics with 85% reversibility at 10.0 MPa H_2, 160 °C.[40] Our previous study showed that $NaAlH_4$ can be reversibly stored with minimal capacity loss when confined within the nanopores of a titanium-functionalized metal–organic framework template. The hydride-loading method, which involved melt infiltration, resulted in $NaAlH_4$ loadings up to 21 wt.%.[41]

To enhance the kinetic properties and prevent thermodynamic destabilization in Li—Mg—N—H systems, utilizing space-confinement, i.e., nanoscale Li—Mg—N—H, is crucial. In this study, we present a promising approach to achieve high-density, improved reversibility, and kinetically enhanced hydrogen storage by fabricating a $Li_2Mg(NH)_2$@reduced graphene oxide (rGO) composite. The process involves first preparing Mg@rGO, converting it to MgH_2@rGO, melt-infiltration of $LiNH_2$ into the composite, and finally cycling under hydrogen to yield $Li_2Mg(NH)_2$@rGO. The MgH_2@rGO serves as a nucleation site for the formation of nanoscale Li—Mg amides and the lightweight rGO protects the functional particles from aggregation during cycling, enabling reversibility with no capacity degradation observed after ten cycles. Our experimental results show that the $Li_2Mg(NH)_2$@rGO composite exhibits a reversible hydrogen capacity of 4.42 wt.%, which is ≈82% of the theoretical capacity. Advanced electronic structure calculations further reveal that the local chemical interactions between rGO and the Mg-amide/Li hydride interface are responsible for the enhanced kinetics of dehydrogenation. This work provides a new strategy for designing metal imide-based composites that exhibit improved reversible hydrogen storage performance with moderate kinetics.

2. Results and Discussion

The synthesis process of $Li_2Mg(NH)_2$@rGO composite is schematically illustrated in **Figure 1**a. First, the Mg/rGO nanocrystals (NCs)-based nanocomposites were synthesized at room temperature from a homogeneous tetrahydrofuran (THF) solution based on an adapted Rieke method.[10,31,42] The newly developed synthetic procedure uses an environmentally friendly precursor based on earth-abundant elements, $MgCl_2$, where the Mg^{2+} reduction reaction occurs in the solution under nanoconfinement using rGO. rGO is added here to minimize inactive mass in the composites and confine the particle size while maintaining high phase purity by introducing a protective barrier.[23] Additional morphology analysis concerning rGO and the as-fabricated Mg particles on rGO is given in Figures S1 and S2 (Supporting Information). These anchored Mg particles on lightweight rGO, followed by the generation of MgH_2 on rGO, provide the nucleation site for Li—Mg amides, which is achieved by a second melt infiltration process in the presence of Li-amides. Due to the confinement effect of rGO, the size of the final $Li_2Mg(NH)_2$@rGO composite is at the nanoscale based on the transmission electron microcopy (TEM) and high-resolution TEM (HRTEM) images (Figure S3, Supporting Information). The nanoparticles are also observed to be highly crystalline. The STEM-HAADF-EDS mapping in Figure 1b indicates a relatively uniform distribution of N and Mg, with a coating of an ultrathin carbon layer reflected by the distribution of elemental carbon (rGO). The uniform elemental composition persisted during the de-/rehydrogenation cycles, suggesting that the rGO layer preserves the agglomeration and inhibits particle growth of $Li_2Mg(NH)_2$ upon subsequent thermal heating during a repeated H_2 adsorption and desorption process.

X-ray diffraction (XRD) patterns shown in **Figure 2**a,b confirm the formation of Mg@rGO, MgH_2@rGO, and $Li_2Mg(NH)_2$@rGO. The dehydrogenation products are also investigated to reveal the potential mechanism behind this reaction. After hydrogenation, no Li_2NH or MgH_2 peaks were observed after multiple cycles. It is noteworthy that the rehydrogenated sample does not regain the structure of the primary components, i.e., $LiNH_2$ and MgH_2, indicating it is thermodynamically favorable for the —NH_2 amino group to bond with Mg rather than Li. XPS data in Figure S4 (Supporting Information) reveals the electrical status of Mg, Li, and N. Finally, the composition was confirmed ICP analysis, which indicates a Mg:Li atomic ratio of roughly 1:2. Furthermore, a comparison of XRD and HRTEM was included and described below: TEM and HRTEM analyses of the hydrogenated $Li_2Mg(NH)_2$@rGO after multiple cycles (Figure 2c,d) suggest that the hydrogenated phases are likely LiH, with a lattice spacing of 2.07 Å corresponding to its (200) facet, and $Mg(NH_2)_2$ with exposed (204) facets, displaying a lattice spacing of 3.64 Å. This comparison provides valuable insights into the structural properties of the materials and supports the conclusions drawn from the XRD analysis.

The original as-synthesized composite undergoes chemical transformation after multiple cycles of hydrogen desorption and rehydrogenation, finally transforming into $(2LiH+1Mg(NH_2)_2)$@rGO, consistent with previous studies on bulk $2LiNH_2$-$1MgH_2$,[18,20,22,43] which conclusively demonstrated

**ADVANCED
SCIENCE NEWS**
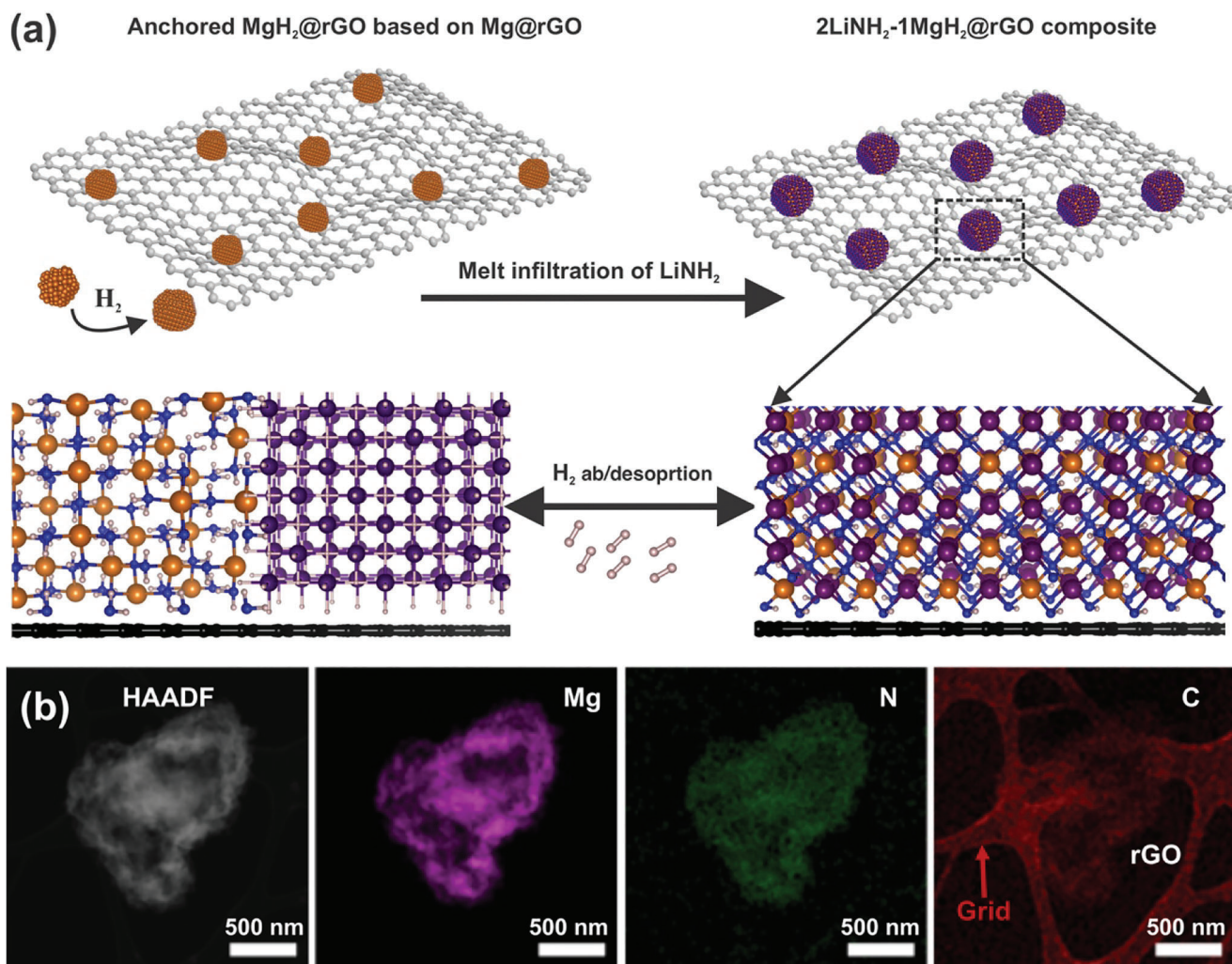
www.advancedsciencenews.com

**ADVANCED
MATERIALS
INTERFACES**
Open Access

www.advmatinterfaces.de

Figure 1. a) Schematic diagram of the synthesis process of $Li_2Mg(NH)_2$@rGO composite. b) STEM-HAADF image with the EDS elemental mapping of the as-synthesized $Li_2Mg(NH)_2$@rGO composite. The high resolution TEM images reflecting the particle size and crystallization status were given in Supporting Information.

that the MgH_2 + $2LiNH_2$ → $Li_2Mg(NH)_2$+$2H_2$ ⇔ $Mg(NH_2)_2$+$2LiH$ reaction is energetically favorable.

The H_2 absorption and desorption curves of $Li_2Mg(NH)_2$@rGO observed in temperature-pressure-desorption (TPD) are shown in **Figure 3**. The hydrogen storage capacity of the material was stabilized at about 4.42 wt.%, which is ≈82% of the theoretical capacity, after five rehydrogenation and dehydrogenation cycles. As shown in Figure 3b, dehydrogenation begins at ≈170 °C, but higher temperatures are required to fully release hydrogen. Further details on the hydrogen desorption during the first and subsequent cycles can be found in Figures S5 and S6 (Supporting Information). Significantly, the rate of hydrogen desorption is significantly improved compared to bulk counterparts, demonstrating the positive impact of rGO on hydrogen desorption.

Kinetic modeling based on the shrinking core model indicates both H_2 diffusion and reaction play roles in the overall desorption kinetics of bulk 2:1 amide materials.[44] Nanosizing shortens the H_2 diffusion paths during dehydrogenation of 2LiH-

$1Mg(NH_2)_2$@rGO, which can potentially enhance the kinetics of H_2 desorption when the process is predominantly controlled by mass transport. The local interaction between the anchored MgH_2 on rGO and melt-infiltrated $LiNH_2$ enables persistently close contact between the $Mg(NH_2)_2$ and LiH phases, so that no long-range diffusion of different phases is needed for the dehydrogenation reactions during cycling.

To gain further insights into the mechanistic origin of the observed kinetics enhancement, we performed first-principles metadynamics simulations to determine the effect of rGO on the dehydrogenation kinetics of $2LiH-Mg(NH_2)_2$. HRTEM images in Figure 2c,d indicate that after multiple cycles, the hydrogenated state was stabilized as $2LiH-Mg(NH_2)_2$ and tertiary interfaces can be observed among LiH (part I), $Mg(NH_2)_2$ (part II), and rGO. To simulate $2LiH-Mg(NH_2)_2$, we adopted a cluster structural model containing four formula units of $2LiH-Mg(NH_2)_2$ that broadly captures both the interfacial interactions and cohesive interactions within each individual phases. The constructed cluster compound was first structurally sampled through 50 ps of simulated
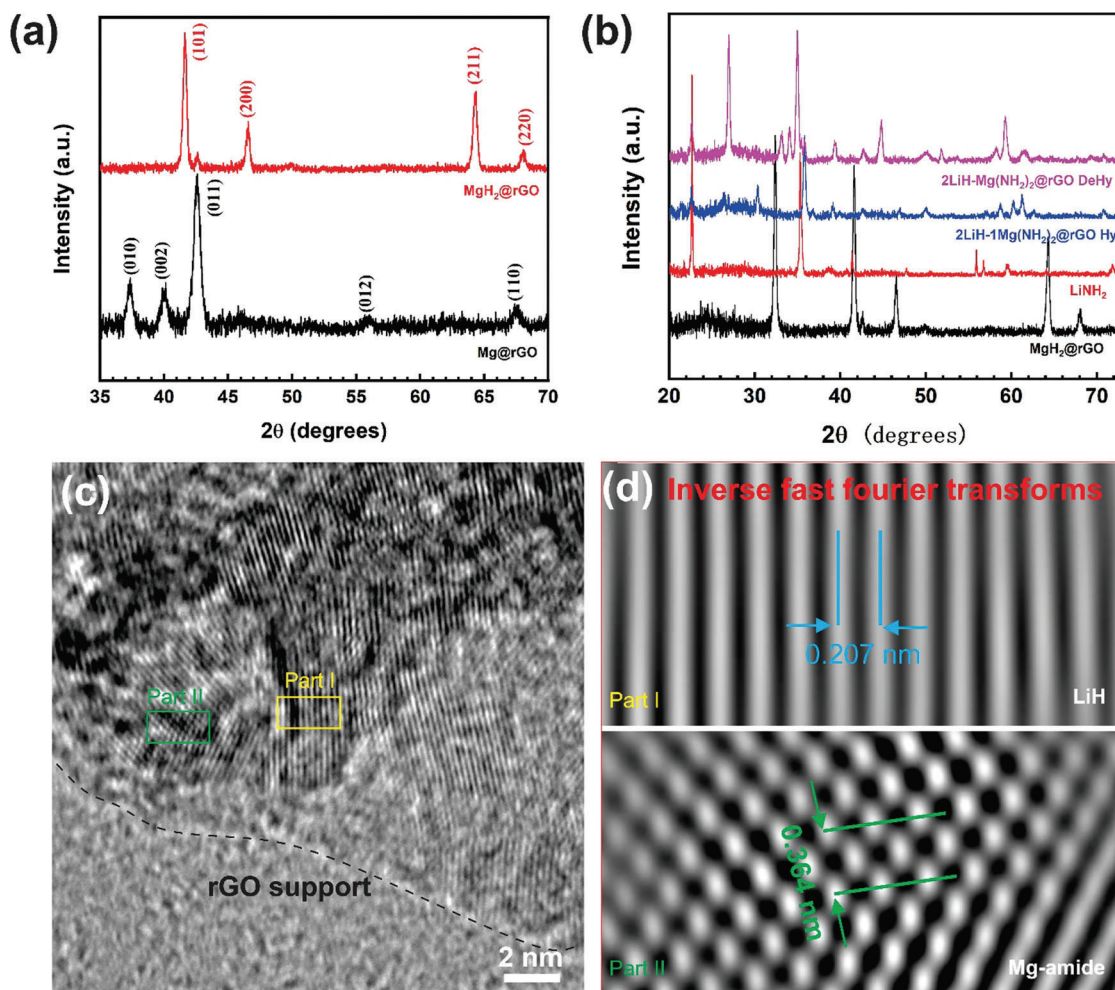
2300310 (3 of 9)

Figure 2. a,b) X-ray diffraction (XRD) patterns confirm the formation of LiNH$_2$-MgH$_2$@rGO composites, as well as individual XRD patterns for Mg@rGO, LiNH$_2$. The XRD patterns of the final products after dehydrogenation and rehydrogenation were provided for comparison. c) Transmission Electron Microscopy (TEM) and d) High-Resolution Transmission Electron Microscopy (HRTEM) analyses were conducted on 2LiNH$_2$-1MgH$_2$@rGO after multiple dehydrogenation cycles.
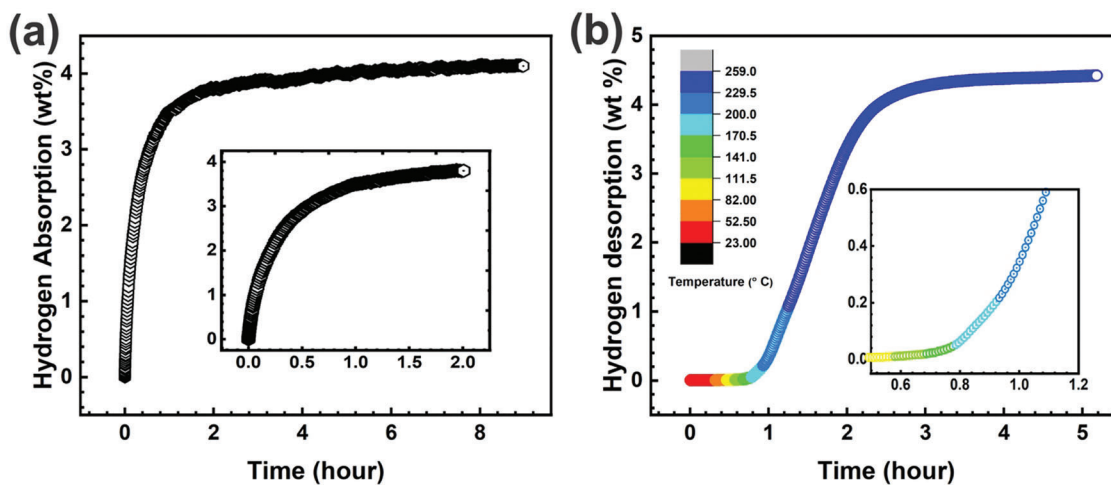

Figure 3. a) The hydrogen absorption rate of Li$_2$Mg(NH)$_2$@rGO under 130 bar hydrogen pressure at 250 °C. The inset shows a zoomed version of the profile, focusing on the rapid hydrogen uptake during the initial 2 h of hydrogenation; b) H$_2$ desorption curve of 2LiH-1Mg(NH$_2$)$_2$@rGO upon heating from room temperature to 259 °C.
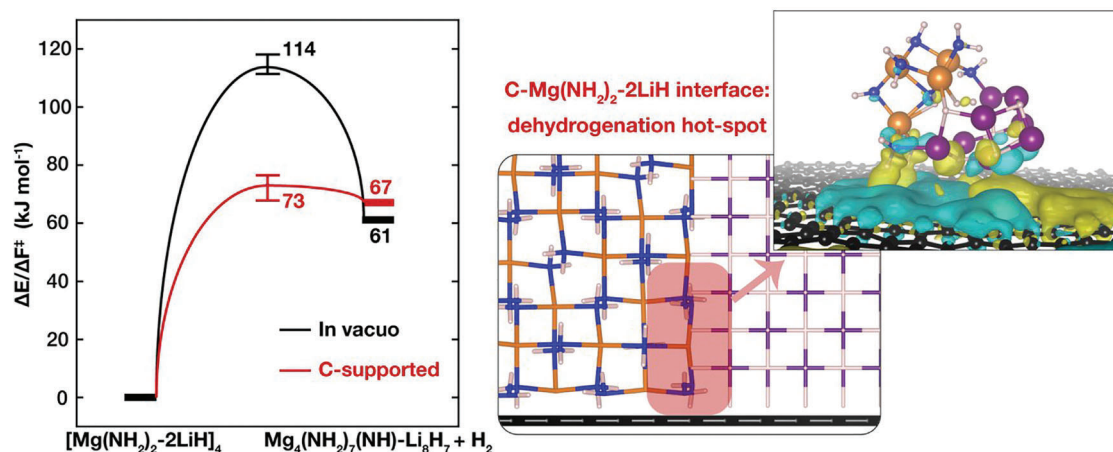
Figure 4. Reaction energies (ΔE) and free energy barriers ($\Delta F^{\ddagger}$) for the interfacial dehydrogenation of 2LiH-Mg(NH$_2$)$_2$ cluster with and without carbon support. $\Delta F^{\ddagger}$ were computed based on metadynamics simulations performed at 473 K. The schematic image on the right shows the hotspots where dehydrogenation takes place initially before propagating along the interface and into the bulk-like regions. The structural snapshot in the course of a metadynamics simulation of a graphene-supported 2LiH-Mg(NH$_2$)$_2$ cluster near its transition state of interfacial dehydrogenation and the associated charge density difference was superimposed. Color scheme for different elements: black-C, orange-Mg, purple-Li, blue-N, and pink-H. Color scheme for isosurfaces: yellow-charge accumulation, cyan-charge depletion. Isosurface level: 0.7×10^{-4}.

annealing using ab initio molecular dynamics. Metadynamics were then run to contrast the interfacial dehydrogenation kinetics of the compound in vacuo, approximating the bulk form, and in proximity of a monolayer graphene sheet, approximating the rGO encapsulated composite.

As shown in **Figure 4**, the free energy barrier for the interfacial dehydrogenation of an unsupported 2LiH-Mg(NH$_2$)$_2$ cluster is fairly high and close to the apparent activation energy for H$_2$ desorption of bulk 2LiNH$_2$-MgH$_2$ reported by Goudy et al.[44] Surprisingly, the presence of the carbon layer as a support lowers the barrier by >40 kJ mol^{-1} even though the reaction energy remains similar to that of the unsupported case. As illustrated in Figure 4, the charge density difference plot of the structural snapshot from a metadynamics trajectory clearly reveals the dipole–dipole interaction between 2LiH-Mg(NH$_2$)$_2$ and graphene near its transition state. The effect of the barrier reduction can be rationalized by the local chemical interactions resulting from the charge redistribution on the 2LiH-Mg(NH$_2$)$_2$ cluster and the graphene substrate upon close contact that stabilize the transition state. These findings suggest that the kinetics of dehydrogenation at the 2LiH-Mg(NH$_2$)$_2$ interface near rGO can be significantly enhanced. These regions are expected to be the kinetic hotspots where dehydrogenation takes place. The reaction yields secondary amines (—NH), which undergo structural reorganization along with Li$^+$ and Mg^{2+} ions, ultimately leading to the formation of the crystalline Li$_2$Mg(NH)$_2$ phase. Complete dehydrogenation from 2LiH-Mg(NH$_2$)$_2$ to Li$_2$Mg(NH)$_2$ under the same mild conditions as observed experimentally requires sustained interfacial reactions throughout the process as neither of the two constituent phases individually undergoes dehydrogenation at temperatures below 300 °C. This suggests that the H-containing molecular units (—NH, —NH$_2$, and H$^-$) exhibit structural mobility in the intermediate phases, allowing their migration and continuous contact between LiH and Mg(NH$_2$)$_2$. Additionally, our TEM images indicate that the encapsulated particles are highly polycrystalline with nanometer-sized crystallites, reducing the

diffusion paths for H-containing molecular units. Therefore, our hypothesis is that persistent rGO/LiH/ Mg(NH$_2$)$_2$ tertiary interfaces exist, where dehydrogenation reactions occur continuously, and the interfaces are replenished through kinetically facile migration of H-containing units between bulk-like and interfacial regions. The local catalytic effect together with the shorter H$_2$ diffusion paths enabled by nanosizing are thus expected to be the main driving forces for the enhanced H$_2$ desorption kinetics of the rGO-encapsulated composite material.

To evaluate the thermodynamic properties for the hydrogen uptake reaction of the Li$_2$Mg(NH)$_2$@rGO composite, pressure-composition isotherms (PCI) were recorded at 233, 241, 250, and 258 °C (Figure 5a). Sloped plateaus are observed across the entire region of hydrogen content. It is noteworthy that the problematic dehydrogenation behavior typically seen in traditional bulk Li-N-H systems (above 1 MPa) has been partially resolved. Additionally, hydrogen is absorbed at a much lower temperature.[15,16] The reaction enthalpy was calculated from the Van't Hoff plots in Figure 5b. The calculated changes of enthalpy (ΔH) and entropy (ΔS) are 42 kJ mol^{-1} H$_2$ and 116 J K^{-1} mol^{-1} H$_2$ that entail an equilibrium pressure of 1 bar at 89 °C. These values represent a significant reduction in ΔH compared to the nanoscale MgH$_2$ system (ΔH of 71.2 kJ mol^{-1} H$_2$, ΔS of 129.6 J K^{-1} mol^{-1} H$_2$ at 276 °C of 1 bar H$_2$) with particle sizes of 2–7 nm.[14] This reduction in ΔH leads to a decrease in the 1 bar hydrogen equilibrium temperature from 276 to 89 °C. The measured ΔH and ΔS values for the Li$_2$Mg(NH)$_2$@rGO material are similar to those reported for bulk materials.[45] This supports the conclusion from metadynamics calculations that the enhancements in hydrogen storage properties are primarily driven by improved kinetics.

Cycle stability serves as a crucial indicator for assessing the potential commercial viability of a hydrogen storage material. Liang et al. conducted a study where the Mg(NH$_2$)$_2$–2LiH material, doped with KOH, underwent 30 cycles of hydrogen release at 230 °C and hydrogen absorption at 210 °C. Their results showed a decrease in hydrogen storage capacity from 5.46% to
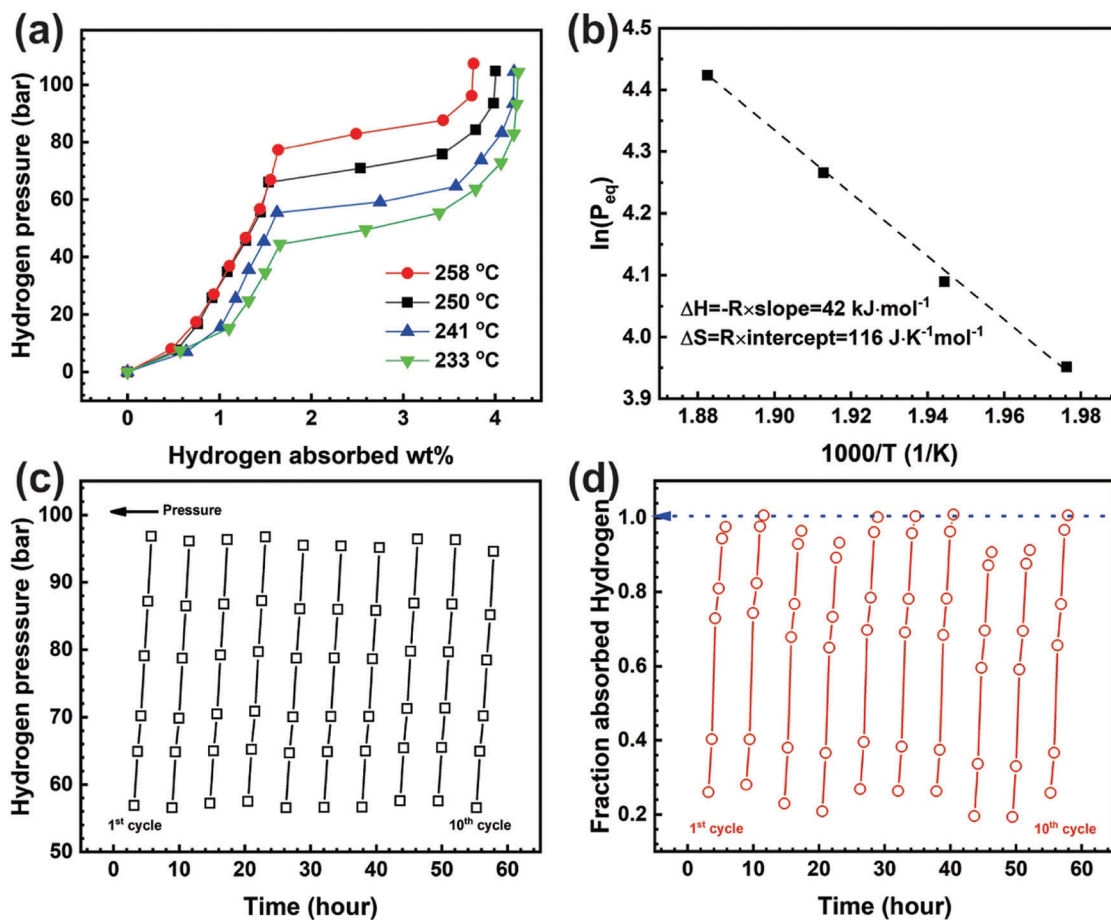
Figure 5. a) Pressure-composition isotherms for $Li_2Mg(NH)_2$@rGO composite decomposition at around 230–260 °C. b) The corresponding Van't Hoff plot based on which the reaction enthalpy/entropy were calculated. c) Pressure data and d) cyclability of $Li_2Mg(NH)_2$@rGO composite. Between each hydrogen absorption cycling, a full evacuation was performed.

5.01% after the cycles, with an average hydrogen storage loss of 0.015% per cycle.[35] To investigate the cycling performance of the $Li_2Mg(NH)_2$/rGO composite, cycling hydrogen absorption measurements were carried out, as depicted in Figure 5c,d. The measurements involved alternating cycles of applying H_2 pressure (individual data points in Figure 5c) and calculating H_2 uptake based on pressure changes at each data point (Figure 5d), followed by sample evacuation before the subsequent absorption cycle. Notably, no signs of capacity degradation were observed even after 10 cycles, indicating the material's suitability for hydrogen storage applications. The release of ammonia gas during the hydrogen absorption and dehydrogenation process has been a persistent challenge hindering the practical use of $Mg(NH_2)_2$–2LiH. Liu et al. highlighted that ammonia emissions during the hydrogen absorption and desorption process of $Mg(NH_2)_2$–2LiH materials are primarily attributed to the decomposition of $Mg(NH_2)_2$.[46] Mass spectrometry (MS) analysis, as shown in Figure S7 (Supporting Information), revealed negligible ammonia release during the dehydrogenation process. This is significant because the release of ammonia is a leading cause of hydrogen capacity decay in bulk amides, as it results in the loss of elemental nitrogen. In this study, the average concentration of ammonia was found to be <0.1% (NH_3/H_2) at 250 °C.

3. Conclusion

In this study, a nanoscale ternary composite $Li_2Mg(NH)_2$@rGO was developed with the aim of improving the hydrogen storage properties of metal amides. The composite is characterized by a weight penalty of only 2 wt.% due to the presence of lightweight graphene oxide (rGO). The results of this study show that the locally anchored MgH_2 nanoparticles on rGO serve as nucleation sites for the formation of mixed-cation Li—Mg amides, leading to a nano-confined $Li_2Mg(NH)_2$@rGO composite. The initial dehydrogenation reaction results in the formation of a Li—Mg—N—H ternary imide ($Li_2Mg(NH)_2$) that can be reversibly rehydrogenated. The presence of rGO acts as a barrier to suppress particle growth and agglomeration during cycling, leading to improved hydrogen storage properties. It is anticipated that persistent interfaces exist among reduced graphene oxide (rGO), LiH, and $Mg(NH_2)_2$, where dehydrogenation reactions occur continuously, and the interfaces are replenished through the easy migration of H-containing units between bulk-like and interfacial regions. The experimental reversible hydrogen capacity for the $Li_2Mg(NH)_2$@rGO composite reaches 4.42 wt.%, which is ≈82% of the theoretical capacity. The results of this study demonstrate that nanoconfinement can lead to significant enhancements in

**ADVANCED
SCIENCE NEWS**

www.advancedsciencenews.com

**ADVANCED
MATERIALS
INTERFACES**
Open Access

www.advmatinterfaces.de

hydrogen storage performance while maintaining high cycle-life and H₂ purity.

Precise control over the placement of reacting species at the nanoscale level can result in accelerated rates of solid-state chemical processes due to the increased proximity to catalytic surfaces. Our first-principle metadynamics modeling supports the idea that the favorable local interaction between rGO and 2LiH/Mg(NH₂)₂ forms kinetic hotspots during the initial interfacial dehydrogenation reaction, thus improving the rate of H₂ desorption. The lightweight nature of rGO makes it an attractive host for creating unique nanoscale hotspots that are separated from the surrounding hydride phase. The acceleration of hydrogen uptake and release kinetics in Li₂Mg(NH)₂@rGO is not the only example of such enhancements; similar improvements in reaction rates have been previously reported in other systems like MgH₂@rGO,[31] Ni-doped MgH₂@rGO,[24] and Mg(BH₄)₂@rGO.[47] The combination of catalytic and nanoconfinement effects demonstrated in this study can be applied to other solid-state energy storage and conversion material systems to enhance interfacial reactions.[48]

4. Experimental Section

The active Mg@rGO were fabricated by using an adapted Rieke method by reducing metal salts in solvents using alkali metals.[10] Specifically, 12 mmol MgCl₂ (1.14 g) were dissolved in 120 mL dry tetrahydrofuran (THF), heated near the boiling point of THF for at least 3 h, after which the mixture was cooled to room temperature. Next, 30 mmol 2-Methylnaphthalene (4.266 g) and 28.6 mmol Li-metal (0.198 g) were dissolved in 33 mL dry THF to form the reducing agent at room temperature. The mixture was gently stirred for 1.5 h at 500 rpm to ensure Li-metal was totally dissolved. Separately, 20 mg GO was dissolved in 30 mL THF and sonicated for 1 h before mixing with the Mg precursors. The mixture was subsequently mixed with Li-2-Methylnaphthalene and allowed to stand for 1.5 h. The mixture becomes dark immediately after the injection of metal precursors, in which lithium-Methylnaphthalene reduces the Mg²⁺ in the presence of rGO. The mixture was centrifuged (9000 rpm, 20 min) and washed three times using dry THF until the supernatant solutions were clear. The final precipitate was vacuum dried in a glovebox overnight to yield a black powder. All experiments were performed under inert atmosphere in an argon-filled glove box (O₂ and H₂O concentration <1 ppm).

The Mg@rGO material was sealed in a stainless-steel container and evacuated for 16 h at 250 °C, then treated with 10.5 MPa hydrogen for 4 h to form MgH₂@rGO. Lithium amide (827 mg, 36.0 mmol) was mixed with 500 mg of as-prepared MgH₂@rGO inside an argon glovebox to achieve a nominal LiNH₂:MgH₂ molar ratio of ≈2.0:1.0. The mixture was then sealed in a stainless-steel container and connected to a manifold using a Swagelok connection. The sample was purged three times using vacuum/argon cycles, then evacuated for 10 min. The sample was then pressurized with 1.2 MPa gaseous ammonia. The sample holder was sealed, then heated to 390 °C and kept for 4 h under ammonia gas to achieve reactive melting of LiNH₂ into the rGO composite. Hydrogenating the as-synthesized hydride/amide/rGO composite under 12 MPa hydrogen at 250 °C, followed by dehydrogenation in vacuum at 250 °C yields Li₂Mg(NH)₂@rGO.

Characterization of the as-prepared samples was performed by X-ray diffraction (XRD) using a Bruker AXS D8 Discover GADDS X-Ray Diffractometer using Co radiation. To minimize the H₂O/O₂ exposure during sample transportation and measurements, the samples were loaded in glass capillaries prior to XRD analysis. The morphology and microstructure of the as-prepared samples were observed using a transmission electron microscope (JEOL 2100-F 200 kV Field-Emission Analytical Transmission Electron Microscope), with an Oxford high solid-angle Silicon Drift Detector X-Ray Energy Dispersive Spectrometer (EDS) system for chemical elemental analysis. X-ray photoelectron spectroscopy (XPS) measurements were performed using a K-Alpha XPS System (Thermo Scientific). Here, the photon source was a monochromatic Al K α line ($h\nu$ = 1486.6 eV). Spectra were acquired using a spot size of 400 μm and constant pass energy. A combined low energy electron/ion flood source was used for charge neutralization. A vacuum transfer vessel was used to protect the sample from oxidation. Inductively Coupled Plasma Atomic Emission Spectroscopy (ICP-AES, Varian ICP-OES 720 Series) analyses were used to confirm the compositions.

The hydrogen absorption and desorption characteristics were evaluated using a pressure-composition-temperature (PCT, PCT-2000) volumetric instrument at different temperatures. The PCT measurements were performed isothermally varying the dose pressure from 0.1 to 20 bar H₂, with equilibration times between 240 and 960 min. To determine the kinetics, the activation energy for hydrogen absorption and desorption were determined from measurements at four different temperatures. The quantitative determination of ammonia was conducted on a Setaram Residual Gas Analyzer. The cycling performance was tested at varies H₂ pressure until reached saturation, after which, a full evacuation was performed before the next cycling.

Ab initio molecular dynamics, metadynamics simulations, and geometry optimization calculations were performed with the Vienna ab initio simulation package (VASP), version 5.4.4,[49] using the projector augmented wave treatment of core−valence interactions [50,51] with the Perdew−Burke−Ernzerhof (PBE)[52] generalized gradient approximation for the exchange-correlation energy and the D3 vdW-dispersion energy-correction.[53,43] A 15 Å × 15 Å × 15 Å cubic box was used to model the isolated amide/hydride cluster with the Brillouin zone sampled at the Γ-point only. The rGO was approximated by a 10 × 10 monolayer graphene sheets containing 128 carbon atoms. The graphene and graphene in contact with an amide/hydride cluster were simulated with a Γ-centered 2 × 2 × 1 k-point mesh. For all calculations, the energy cutoff for the plane-wave basis set was set to 400 eV, self-consistent-field electronic energies were converged to 10^{-4} eV. For geometry optimizations, all atomic forces were minimized to be <0.03 eV Å⁻¹. Bader charge analyses were performed using the algorithm developed by Henkelman et al.[54] Hydrogen atoms were modeled as deuterium to allow a timestep of 1 fs and a Nose−Hoover thermostat was used to maintain the temperature at 473 K, a typical H₂ desorption temperature for the material system, for the dynamic simulations. Metadynamics is a nonequilibrium molecular dynamics method capable of efficiently sampling free energy surfaces of complex reactions.[55] The coordination number of a pair of H atoms at the LiH and Mg(NH₂)₂ interface as the collective variable (CV), mathematically defined as

$$\frac{1 - \left(\frac{d_{ij}}{d_0}\right)^9}{1 - \left(\frac{d_{ij}}{d_0}\right)^{14}} \tag{5}$$

where d_{ij} is the actual distance between H atom i and j, and d_0 is the reference distance as the boundary of being bonded or not between the two atoms, which was set to be 1 Å. The height of each biasing gaussian potential was set to 0.005 eV and the width 0.02. Biasing potentials were introduced every 40 timesteps, i.e., 40 fs. Following a previously established protocol,[56] we terminated a run of metadynamics simulation after the first barrier crossing from the reactant basin into the target product basin and computed the free energy barrier by summing up the number of bias potentials accumulated in the reactant basin. Error bars associated each free energy barrier were computed based on three replicas starting with different initial configurations.

Supporting Information

Supporting Information is available from the Wiley Online Library or from the author.

Conflict of Interest

The authors declare no conflict of interest.

Data Availability Statement

The data that support the findings of this study are available from the corresponding author upon reasonable request.

[1] J. A. Turner, *Science* **1999**, *285*, 687.
[2] G. Xie, K. Zhang, B. Guo, Q. Liu, L. Fang, J. R. Gong, *Adv. Mater.* **2013**, *25*, 3820.
[3] T. He, P. Pachfule, H. Wu, Q. Xu, P. Chen, *Nat. Rev. Mater.* **2016**, *1*, 16067.
[4] M. D. Allendorf, V. Stavila, J. L. Snider, M. Witman, M. E. Bowden, K. Brooks, B. L. Tran, T. Autrey, *Nat. Chem.* **2022**, *14*, 1214.
[5] P. Prachi R, W. Mahesh M, G. Aneesh C, *Adv. Energy Power* **2016**, *4*, 11.
[6] L. Schlapbach, A. Züttel, *Nature* **2001**, *414*, 353.
[7] R. Mohtadi, S. I. Orimo, *Nat. Rev. Mater.* **2016**, *2*, 16091.
[8] N. A. A. Rusman, M. Dahari, *Int. J. Hydrogen Energy* **2016**, *41*, 12108.
[9] Q. Wang, J. Guo, P. Chen, *Joule* **2020**, *4*, 705.
[10] K. J. Jeon, H. R. Moon, A. M. Ruminski, B. Jiang, C. Kisielowski, R. Bardhan, J. J. Urban, *Nat. Mater.* **2011**, *10*, 286.
[11] C. Dun, S. Jeong, D.-H. Kwon, S. Kang, V. Stavila, Z. Zhang, J.-W. Lee, T. M. Mattox, T. W. Heo, B. C. Wood, J. J. Urban, *Chem. Mater.* **2022**, *34*, 2963.
[12] T. Sadhasivam, H. T. Kim, S. Jung, S. H. Roh, J. H. Park, H. Y. Jung, *Renew Sustain Energy Rev* **2017**, *72*, 523.
[13] X. L. Zhang, Y. F. Liu, X. Zhang, J. J. Hu, M. X. Gao, H. G. Pan, *Mater. Today Nano* **2020**, *9*, 100064.
[14] M. Paskevicius, D. A. Sheppard, C. E. Buckley, *J. Am. Chem. Soc.* **2010**, *132*, 5077.
[15] C. Ping, X. Zhitao, L. Jizhong, L. Jianyi, T. Kuang Lee, *Nature* **2002**, *420*, 20.
[16] W. I. F. David, M. O. Jones, D. H. Gregory, C. M. Jewell, S. R. Johnson, A. Walton, P. P. Edwards, *J. Am. Chem. Soc.* **2007**, *129*, 1594.
[17] K. Hoang, A. Janotti, C. G. Van De Walle, *Phys. Rev. B* **2012**, *85*, 064115.
[18] Z. Xiong, G. Wu, J. Hu, P. Chen, *Adv. Mater.* **2004**, *16*, 1522.
[19] C. Zhang, A. Alavi, *J. Phys. Chem. B* **2006**, *110*, 7139.
[20] W. Luo, V. Stavila, L. E. Klebanoff, *Int. J. Hydrogen Energy* **2012**, *37*, 6646.
[21] B. Zhang, Y. Wu, *Prog. Nat. Sci.: Mater. Int.* **2017**, *27*, 21.
[22] J. Hu, M. Fichtner, *Chem. Mater.* **2009**, *21*, 3485.
[23] S. Garroni, A. Santoru, H. Cao, M. Dornheim, T. Klassen, C. Milanese, F. Gennari, C. Pistidda, *Energies* **2018**, *11*, 1027.
[24] C. Liang, M. Gao, H. Pan, Y. Liu, *Appl. Phys. Lett.* **2014**, *105*, 083909.
[25] N. S. Gamba, G. Amica, P. A. Larochette, F. C. Gennari, *Int. J. Hydrogen Energy* **2017**, *42*, 6024.
[26] E. S. Cho, A. M. Ruminski, Y. S. Liu, P. T. Shea, S. Y. Kang, E. W. Zaia, J. Y. Park, Y. De Chuang, J. M. Yuk, X. Zhou, T. W. Heo, J. Guo, B. C. Wood, J. J. Urban, *Adv. Funct. Mater.* **2017**, *27*, 1704316.
[27] B. C. Wood, V. Stavila, N. Poonyayant, T. W. Heo, K. G. Ray, L. E. Klebanoff, T. J. Udovic, J. R. I. Lee, N. Angboonpong, J. D. Sugar, P. Pakawatpanurut, *Adv. Mater. Interfaces* **2017**, *4*, 1600803.
[28] C. Dun, S. Jeong, Y. Liu, N. Leick, T. M. Mattox, J. Guo, J. Lee, T. Gennett, V. Stavila, J. J. Urban, *Small* **2021**, *17*, 2101989.
[29] Y. Cho, S. Li, J. L. Snider, M. A. T. Marple, N. A. Strange, J. D. Sugar, F. El Gabaly, A. Schneemann, S. Kang, M. H. Kang, H. Park, J. Park, L. F. Wan, H. E. Mason, M. D. Allendorf, B. C. Wood, E. S. Cho, V. Stavila, *ACS Nano* **2021**, *15*, 10163.
[30] V. Stavila, S. Li, C. Dun, M. A. T. Marple, H. E. Mason, J. L. Snider, J. E. Reynolds, F. El Gabaly, J. D. Sugar, C. D. Spataru, X. Zhou, B. Dizdar, E. H. Majzoub, R. Chatterjee, J. Yano, H. Schlomberg, B. V. Lotsch, J. J. Urban, B. C. Wood, M. D. Allendorf, *Angew. Chem., Int. Ed.* **2021**, *60*, 25815.
[31] E. S. Cho, A. M. Ruminski, S. Aloni, Y. S. Liu, J. Guo, J. J. Urban, *Nat. Commun.* **2016**, *7*, 10804.
[32] A. Schneemann, L. F. Wan, A. S. Lipton, Y. S. Liu, J. L. Snider, A. A. Baker, J. D. Sugar, C. D. Spataru, J. Guo, T. S. Autrey, M. Jørgensen, T. R. Jensen, B. C. Wood, M. D. Allendorf, V. Stavila, *ACS Nano* **2020**, *14*, 10294.
[33] J. L. White, N. A. Strange, J. D. Sugar, J. L. Snider, A. Schneemann, A. S. Lipton, M. F. Toney, M. D. Allendorf, V. Stavila, *Chem. Mater.* **2020**, *32*, 5604.
[34] A. Schneemann, J. L. White, S. Kang, S. Jeong, L. F. Wan, E. S. Cho, T. W. Heo, D. Prendergast, J. J. Urban, B. C. Wood, M. D. Allendorf, V. Stavila, *Chem. Rev.* **2018**, *118*, 10775.
[35] C. Liang, Y. Liu, M. Gao, H. Pan, *J. Mater. Chem. A* **2013**, *1*, 5031.
[36] D. E. Demirocak, S. S. Srinivasan, M. K. Ram, J. N. Kuhn, R. Muralidharan, X. Li, D. Y. Goswami, E. K. Stefanakos, *Int. J. Hydrogen Energy* **2013**, *38*, 10039.
[37] C. Li, Y. Liu, Y. Yang, M. Gao, H. Pan, *J. Mater. Chem. A* **2014**, *2*, 7345.
[38] Y. Luo, Q. Wang, J. Li, F. Xu, L. Sun, Y. Zou, H. Chu, B. Li, K. Zhang, *Mater. Today Nano* **2020**, *9*, 100071.
[39] Y. Sun, C. Shen, Q. Lai, W. Liu, D. Wang, *Energy Storage Mater.* **2018**, *10*, 168.
[40] F. E. Pinkerton, *J. Alloys Compd.* **2011**, *509*, 8958.
[41] V. Stavila, R. K. Bhakta, T. M. Alam, E. H. Majzoub, M. D. Allendorf, *ACS Nano* **2012**, *6*, 9807.
[42] N. S. Norberg, T. S. Arthur, S. J. Fredrick, A. L. Prieto, *J. Am. Chem. Soc.* **2011**, *133*, 10679.
[43] S. Grimme, S. Ehrlich, L. Goerick, *J. Comput. Chem.* **2012**, *32*, 174.
[44] T. Durojaiye, J. Hayes, A. Goudy, *Int. J. Hydrogen Energy* **2015**, *40*, 2266.

[45] J. Wang, T. Liu, G. Wu, W. Li, Y. Liu, C. M. Araújo, R. H. Scheicher, A. Blomqvist, R. Ahuja, Z. Xiong, P. Yang, M. Gao, H. Pan, P. Chen, *Angew. Chem., Int. Ed.* **2009**, *48*, 5828.

[46] Y. Liu, J. Hu, G. Wu, Z. Xiong, P. Chen, *J. Phys. Chem. C* **2008**, *112*, 1293.

[47] S. Jeong, T. W. Heo, J. Oktawiec, R. Shi, S. Kang, J. L. White, A. Schneemann, E. W. Zaia, L. F. Wan, K. G. Ray, Y. S. Liu, V. Stavila, J. Guo, J. R. Long, B. C. Wood, J. J. Urban, *ACS Nano* **2020**, *14*, 1745.

[48] E. Pomerantseva, F. Bonaccorso, X. Feng, Y. Cui, Y. Gogotsi, *Science* **2019**, *366*, 969.

[49] G. Kresse, J. Furthmüller, *Phys. Rev. B* **1996**, *54*, 11169.

[50] P. Blöchl, *Phys. Rev. B* **1994**, *50*, 17953.

[51] G. Kresse, D. Joubert, *Phys. Rev. B* **1999**, *59*, 1758.

[52] J. P. Perdew, K. Burke, M. Ernzerhof, *Phys. Rev. Lett.* **1996**, *77*, 3865.

[53] S. Grimme, J. Antony, S. Ehrlich, H. Krieg, *J. Chem. Phys.* 154104, **2010**, *132*.

[54] W. Tang, E. Sanville, G. Henkelman, *J. Phys. Condens. Matter* **2009**, *21*, 084204.

[55] A. Laio, A. Rodriguez-Fortea, F. L. Gervasio, M. Ceccarelli, M. Parrinello, *J. Phys. Chem. B* **2005**, *109*, 6714.

[56] S. Li, Y. Zheng, F. Gao, J. Szanyi, W. F. Schneider, *ACS Catal.* **2017**, *7*, 5087.